AIAA AVIATION Forum
5-9 June 2017, Denver, Colorado
35th AIAA Applied Aerodynamics Conference

10.2514/6.2017-4456



# Undeflected Common Research Model (uCRM): An Aerostructural Model for the Study of High Aspect Ratio Transport Aircraft Wings

Timothy R. Brooks, * Gaetan K. W. Kenway, † Joaquim R. R. A. Martins, ‡
*University of Michigan, Department of Aerospace Engineering, Ann Arbor, Michigan, United States*

**Since its introduction, the NASA Common Research Model (CRM) has served as a useful aerodynamic benchmark for CFD-based drag prediction and aerodynamic design optimization. The model was originally conceived as a purely aerodynamic benchmark and as such, the wing geometry corresponds to the deflected shape at the nominal 1 g flight condition. There has been growing interest in extending this model for aeroelastic studies. Due to its predefined deflection, the model is not suitable for aeroelastic analysis and design. To address this issue, we define an undeflected Common Research Model (uCRM), which includes the outer mold line geometry of the undeflected wing and the corresponding internal wingbox structure. The developed aeroelastic model achieves the flying shape of the CRM under the nominal flight condition. The topology of the wingbox is designed to be similar to that of a Boeing 777. The jig shape was obtained through an inverse design procedure where the objective was to minimize the difference between the 1 g aerostructurally deflected shape and the CRM. The original CRM has an aspect ratio of 9, so we refer to this model as the uCRM-9. Additionally, since modern transport aircraft are trending toward higher aspect ratio wing designs to reduce induced drag, and therefore fuel burn, there is a need for a higher aspect ratio variant of this model to assess next-generation wings. This variant, the uCRM-13.5, has a larger aspect ratio of 13.5 and is defined through a multipoint aerostructural optimization subject to buffet onset constraints. These models provide a publicly available benchmark for aeroelastic wing analysis and design optimization studies.**



## I. Introduction

Modern Reynolds Averaged Navier–Stokes (RANS) computational fluid dynamics (CFD) solvers feature a variety of turbulence models and parameters that differ from solver to solver. These modeling differences may result in small solution differences for the same geometry and flight condition depending on which solver is used. To validate and compare different CFD solvers, a number of benchmark geometries have been developed. These benchmarks include geometries such as the ONERA M6 wing [33], the German Aerospace Research Center DLR-F4, and the NASA Common Research Model (CRM). The CRM was developed to be representative of a long-range twin-aisle transport aircraft configuration and used in the AIAA Drag Prediction Workshops (DPW) since 2008 [40]. The CRM geometry features a fuselage, wing, and horizontal tail.

Since the CRM was originally intended for the validation of various CFD tools, the geometry of the wing was designed to match the deflected state of the configuration under a nominal 1 g cruise condition. This is ideal from the aerodynamic analysis point of view, since it eliminates the need to find the aeroelastically deformed shape experienced during the flight condition. For aerodynamic shape optimization, where the drag for a single flight condition is minimized, a single flying shape is also acceptable. However, when considering aerodynamic shape optimization considering multiple design points, using a single rigid shape is no longer appropriate, since different flight conditions yield different wing shapes. Thus, even for a purely aerodynamic analysis, aeroelastic effects may need to be taken into consideration. Keye et al. [22] shows significant aeroelastic deformations in the wind tunnel test of the CRM model, and furthermore, to accurately predict the drag polar, these aeroelastic deformations must be accounted for in the CFD analysis.

Despite the challenges mentioned above, a series of aerodynamic shape optimization cases based on the 1 g deflected shape of the CRM wing have been considered for the Aerodynamic Design Optimization Discussion Group (ADODG) benchmarks [8, 9, 18, 24, 28, 35, 39]. Many of these works found that single design point aerodynamic optimization lead to results with poor off-design performance and that multiple flight conditions must be considered

*Ph.D. Candidate, Department of Aerospace Engineering, AIAA Student Member
†Research Investigator, Department of Aerospace Engineering, AIAA Member
‡Professor, Department of Aerospace Engineering, AIAA Associate Fellow

to lead to a practical and robust design [24, 28]. More recently, several optimization cases featuring multiple design conditions were also defined and solved [18, 25]. These benchmark cases have been successful in getting practitioners from academia and industry to solve the same problem. Herein, we aim to leverage the efforts invested into the validation, verification, and design optimization of the CRM wing by developing the undeflected Common Research Model (uCRM) aerostructural benchmarks.

While the application of numerical optimization offers promising results for aerodynamic wing design it is not without drawbacks. To capture the inherent coupling between the structural response and the aerodynamics of the wing at these various flight conditions an aeroelastic model is required. There has been some recent interest in using the CRM configuration as a model for aerostructural (static aeroelastic) as well as aeroelastic and aeroservoelastic analysis and design. The transonic conditions for which the CRM was designed for makes it an ideal model for an aeroelastic benchmark. A number of aeroelastic studies featuring optimization have been conducted based on the CRM geometry using panel methods [12, 34]. This includes the work of Klimmek [23], in which an aeroelastic model for the CRM was developed using an inverse design optimization to recover the jig geometry. While low-fidelity models come with the benefit of lower computational cost, they come with added risk of the optimizer exploiting the physics missing from the model. One example of missing physics was observed by Kenway and Martins [17], where for an Euler-based aerostructural optimization, the design converged to an excessively thick airfoil near the root of the wing. When this model was analyzed using a RANS-based solver, the performance was worse than the initial design due to shock induced separation effects that the Euler model missed.

There have also been a number of efforts utilizing higher fidelity static aerostructural optimization, featuring a RANS-based CFD solver coupled with a computational structural mechanics (CSM) solver using the aspect ratio (AR) 9 model that we develop in this work, the uCRM-9 [6, 20, 26]. Due to a continual push for increased aircraft efficiency and reduction in fuel burn, there has also been growing interest in enabling high aspect ratio wings through the use of future technologies such as tow-steered composites [3, 4], morphing trailing edge wings [7], and additive manufactured wingbox topologies [10]. Each of these studies was conducted using the 13.5 AR model ( uCRM-13.5) developed in this work.

While these studies showed a marked improvement in performance robustness over the single point design, they neglected buffet, which is an aspect critical to transonic wing design. Buffet is an aerodynamic instability that leads to flow separation over the upper surface of the wing. The primary cause for buffet is that as the shocks over the upper surface of the wing increase in strength, due to either an increase in lift coefficient or Mach number, the shocks begin to interact with the boundary layer of the wing causing separation of the flow in an unsteady manner. It is desirable to ensure a sufficient margin between buffet onset and the nominal operating cruise envelope to ensure the ability to maneuver, increasing lift, without experiencing buffet. This constraint is usually active for transonic aircraft. Recent work by Kenway and Martins [16] has shown that by including buffet onset as a constraint, much of the improvement made by the optimizer without the constraint was reduced once the constraint was added. Thus, buffet onset must be considered to achieve a practical wing design.

Because of the growing interest in aerostructural analysis and optimization on the CRM model and future high aspect ratio wing designs, we would like to standardize two aerostructural benchmark geometries: an aspect ratio 9 wing based on the CRM, the *uCRM-9*, and a higher aspect ratio (13.5), variant, the *uCRM-13.5*. Since aerostructural analyses will be performed using these models, the 1 g "built-in" deflections become problematic and we must instead define the jig (undeformed) shape. The goal is that these models provide a useful benchmark for aeroelastic studies. To this end, all files associated with these designs—both geometry and mesh files—are publicly available at `http://mdolab.engin.umich.edu/content/ucrm`. We start this paper by describing the uCRM-9 geometry and structural wingbox model. We then describe the procedure for developing the uCRM-13.5.

## II. Computational Framework

To accurately assess the aeroelastic performance of flexible wing designs, such as the CRM geometry, a framework featuring a tightly coupled high-fidelity aerodynamic and structural mechanics solver is required. To this end, the work in this paper was conducted using the MACH (MDO for Aircraft Configurations with High fidelity) framework [19]. Through the remainder of this section, we briefly describe the components consisting of this framework. Kennedy and Martins [13] and Kenway et al. [19] provide more detailed descriptions of this framework. For the purposes of high-fidelity aeroelastic analysis, this framework is comprised of both a RANS-based CFD and structural finite element solver. The two solvers are coupled by a CFD mesh warping algorithm, which is used to propagate the structural deflections of the wing to the CFD volume mesh. The framework also allows for the variations in the wing geometry by utilizing a shape parametrization algorithm that allows for the perturbation of aerodynamic and structural shape of the wing during the optimization. Lastly, a gradient-based optimizer utilizes the coupled derivatives computed using

an adjoint methods to solve the optimization problem. The MACH framework has proven effective in a number of aerostructural design optimization studies [4, 7, 17, 26].

### A. Aerodynamic Solver

A high-fidelity CFD solver is necessary for capturing the full physics of the aerodynamics. For this reason a second order finite-volume CFD solver, ADflow (formerly SUmb) [27], is included in the MACH framework. ADflow is capable of solving the steady RANS equations on structured multiblock and overset meshes. A single equation Spalart–Allmaras (SA) turbulence model is considered in this work. ADflow is used to compute the aerodynamic forces, such as lift, drag, and moment. Through the use of a discrete adjoint implementation, developed by Mader et al. [30] and Lyu et al. [27] using automatic differentiation (AD), derivatives of aerodynamic functions of interest with respect to large numbers of design variables are computed efficiently.

### B. Structural Solver

To accurately compute the aeroelastic deflection of the wing a high-fidelity structural solver is also required. The structural solver used in the MACH framework is the Toolkit for Analysis of Composite Structures (TACS) [14]. TACS is a CSM solver that was specifically designed for solving structures consisting of thin shell components, which are typical in aerospace structures. The solver employs a parallel direct factorization method, which allows it to efficiently and accurately solve the poorly conditioned structural problems that are inherent in thin shells. In addition to computing the structural displacements, TACS computes other structural functions of interest, such as material failure and buckling loads. Like its aerodynamic counterpart, TACS features an efficient adjoint method for computing structural sensitivities.

### C. Mesh Movement

A mesh movement algorithm is required to perform aerostructural analysis. The purpose of the mesh movement is to take the displacements on the surface of the wing computed from the structural solver and extrapolate them through the volume of the CFD mesh. The main mesh movement algorithm used in MACH is an inverse distance weighting method, like that described by Uyttersprot [37]. This method has the benefit of preserving the mesh quality near surfaces, which is necessary for capturing boundary layer effects.

### D. Aerostructural Solver

To solve aerostructural problems, there must be a coupling scheme between the structural and aerodynamic solvers. In MACH, this discipline coupling is accomplished through a Gauss–Seidel iteration. First, the tractions due to the aerodynamic loads are solved using ADflow. These loads are then applied to the TACS finite-element model from which the displacements of the wing can be calculated along with structural functions of interest, such as buckling and failure. The structural displacements are then transferred to the nodes on the surface of the wing in the CFD mesh using a system of rigid links, as proposed by Brown [5]. The displacements at the surface nodes are then extrapolated to the rest of the nodes throughout the CFD volume mesh using the mesh movement algorithm mentioned above. The aerodynamics is solved again for the new mesh, and the process is repeated until convergence. As with the previous solvers, the aerostructural solver is capable of assembling the coupled adjoint from the adjoint of each discipline, structures and aerodynamics to evaluate the coupled aerostructural derivatives required to solve the design optimization problem.

### E. Geometric Parametrization

For the optimization, the wing shape and planform are parametrized through a free form deformation (FFD). The implementation is that of Kenway and Martins [17]. The surface of wing is embedded in a volume with control points distributed over its surface. As the control points are moved, the shape inside the volume deforms in a continuous manner, giving the optimizer effective control over the cross-sectional shape, twist, and planform (sweep and span) of the wing. There is an additional smaller sub-FFD that encloses the horizontal stabilizer, which allows for control over its incidence in order to trim the aircraft. An example of the FFD model used for this work is shown in Figure 1. In total, there are 240 control points distributed on the surface of this FFD volume to parameterize the wing geometry.

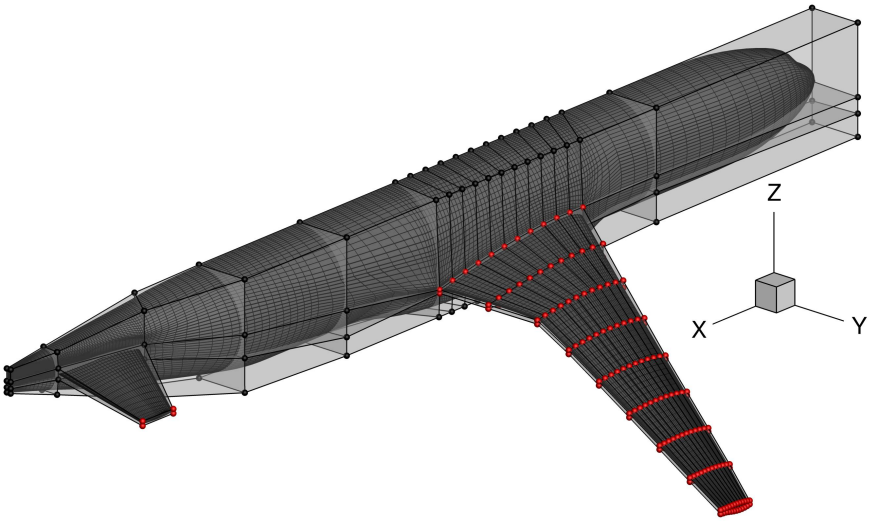


Figure 1: Free form deformation (FFD) volume used for this work; the control points modified by the optimization are shown as red spheres

### F. Optimizer

Aerostructural design problems typically feature large sparse constraint Jacobian. Therefore, it is desirable to use an optimizer that takes advantage of the sparse nature of the problem. For this reason all optimization problems in this work are solved using SNOPT (Sparse Nonlinear OPTimizer) [11], a quasi-Newton gradient-based optimizer that works well for optimization problems featuring large numbers of sparse nonlinear constraints. The optimization tool is wrapped using the Python interface pyOPT [31].

## III. Buffet Constraint

As mentioned previously, buffet occurs when a shock wave oscillates in position due to an interaction with the separated boundary layer. These oscillations grow and eventually become unstable. This unsteady phenomenon leads to undesirable effects, such as flow separation and intense structural vibrations. By its very definition, buffet is inherently an unsteady phenomenon and to accurately model it would require expensive unsteady aerodynamic simulations. In this work, we use a separation-based buffet onset prediction metric based on steady CFD that has shown to be valid for the CRM by Kenway et al. [21]. They found that buffet was correlated with the amount of separated flow, and that for the CRM, buffet onset occurs when 4% of the wing reference area is separated, so we use this value for our buffet onset constraint.

## IV. uCRM-9 Definition

For both the uCRM-9 and the uCRM-13.5, we only model the structure of the wingbox. We had to design a jig shape and structural model for the wing, since no such model currently exists. We designed uCRM-9 model with a jig shape and structure that deforms into the shape of the original outer mold line (OML) of the CRM model at a nominal cruise condition ($M = 0.85$, $C_L = 0.5$ at 37 000 ft) [38]. This structural design was done through an inverse design procedure. First, we defined a wingbox layout based on a similar aircraft, and sized the structure using representative aerodynamic loads. We then applied an inverse design procedure that iteratively removed the deflection from the OML and wingbox geometry, while updating the structural sizing to ensure that the aeroelastically deflected shape matched the nominal deflection profile of the CRM. This is similar to the design procedure used by Kenway et al. [20] with a few key differences. In the original work, the stiffeners were not modeled in the wingbox structural model, while in this work there are modeled using a smeared stiffness approach. In addition, when we size the wingbox, we enforce buckling constraints for all the maneuver loads, whereas in the previous work only material failure was considered. Finally, the aerodynamic model used for this work uses a finer mesh and includes the horizontal stabilizer in the geometry.

### A. Wingbox Structural Definition

As the first step of the uCRM-9 design process, we start by defining a realistic wingbox layout. Due to the proprietary nature of internal wing structures, there is no publicly available data on wingboxes for modern transport aircraft. We based our layout on cutaway views of the Boeing 777-200ER aircraft, since it is the most similar aircraft to the CRM in terms of size and performance. Figure 2 shows the planform view of the 777-200ER extracted from the aircraft planning document [2] with a best-guess superimposed wingbox locations (left), as well as the planform of the CRM and our wingbox layout (right). Using digital versions of the Boeing 777 drawing, we estimate that the extent of the wingbox at the root and tip. We then round off the measurements to obtain the percentage locations with respect to the local chord listed in Table 1. This information was sufficient to define the wingbox structure planform for the CRM geometry. We generate the wingbox for the CRM using the same proportions (front and rear spar location, rib spacing, etc.) and structural layout of the Boeing 777 wingbox. Due to differences in sweep and span, we could not implement the approximated wingbox layout for the Boeing 777 directly in the CRM planform.

The CRM wingbox is composed of an upper and lower skin, two spars, 49 ribs, and an engine mount panel. The leading edge spar is straight, except for a kink at the wing-body junction, while the trailing edge spar features an additional slight kink at the Yehudi break. The center wingbox section includes 4 ribs oriented parallel to the fuselage, while the remaining 45 ribs are distributed along the span of the wing perpendicular to the leading edge, with the exception of the close out rib at the tip. We include an additional panel between two ribs at the Yehudi break. This panel is used to mount the engine to the wing, along with the leading edge spar at this location.

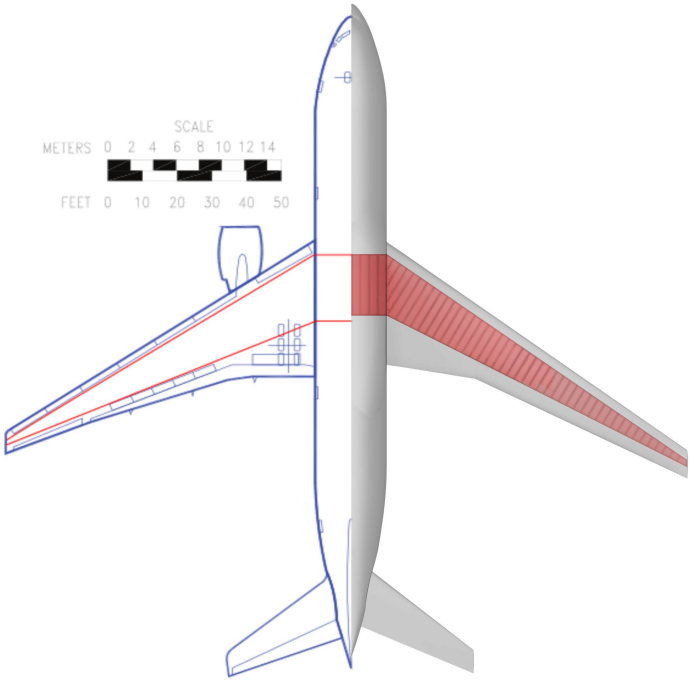


Figure 2: Boeing 777 (left) and uCRM-9 (right). The CRM has a slightly lower wing area and span, and more sweep than the Boeing 777.

Table 1: Spar locations (in % local chord) estimated for the Boeing 777 wingbox and values used for the uCRM-9 wingbox.

| | 777 estimated (%) | uCRM-9 (%) |
|---|---|---|
| Leading edge spar root | 10.4 | 10 |
| Leading edge spar tip | 36.1 | 35 |
| Trailing edge spar root | 59.6 | 60 |
| Trailing edge spar tip | 60.7 | 60 |

Once we defined the planform of the wingbox, we used an in-house tool to generate the geometry of the wingbox

and its components conforming with the wing OML. Figure 3 shows the final wingbox for the CRM. We used a commercial grid generation tool to generate surface meshes for the wingbox geometry. The FEM mesh used for this model consists of 10 285 shell elements with a total of 156 826 degrees of freedom.

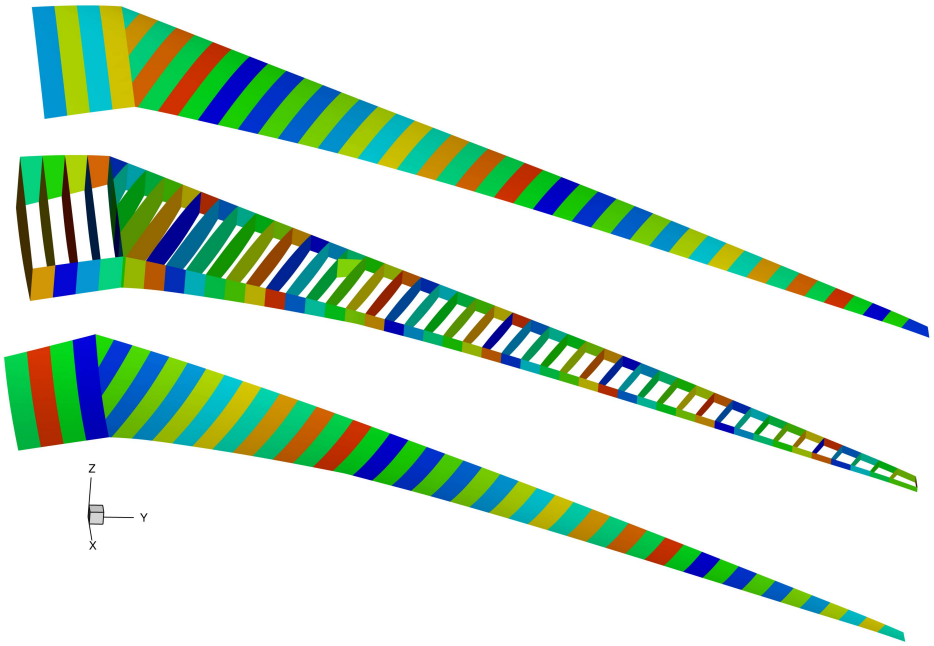


Figure 3: uCRM-9 wingbox geometry.

### B. Aerodynamic Loads

We use a fixed aerodynamic load distribution to recover the undeflected shape of the wing. This aerodynamic load distribution was generated on the CRM wing-body-tail configuration at its nominal cruise condition using meshes from the 5th Drag Prediction Workshop, but with a flight Reynolds number matching the full scale aircraft, as opposed to wind tunnel conditions. The CFD mesh used for this model consists of 5.92 million volume cells. Figure 4 shows the CRM mesh and $C_p$ distribution for the nominal flight condition. We then store the converged aerodynamic pressure and skin friction forces as tractions (force per unit area). For the inverse design procedures, we only apply these tractions to the wingbox, since the other components of the design are assumed to be rigid.

### C. Structural Model Sizing

Once we fix the aerodynamic loads, the wingbox components are sized through numerical optimization. All components in the wingbox structure were modeled using aluminum 7000 series alloy, whose properties are listed in Table 2.

Table 2: Wingbox material properties.

| Parameter | Value |
|---|---|
| Density | 2780 kg/m$^3$ |
| Modulus | $73.1\times10^9$ Pa |
| Poisson Ratio | 0.33 |
| Yield Strength | $420\times10^6$ Pa |

Like all modern transport aircraft, our wingbox uses blade stiffened panels for the main components. The stiffeners are not included explicitly in the FEM model of the wingbox. Instead, we model the effect of their stiffness by homogenizing (or smearing) them into the wingbox panels stiffness. Kennedy et al. [15] describes the smeared stiffness approach in more detail. Figure 5 shows the assumed general cross-section of a wingbox panel under the smeared stiffness approach, where we link the blade and flange thicknesses ($t_w = t_b$) and the blade height to the flange width

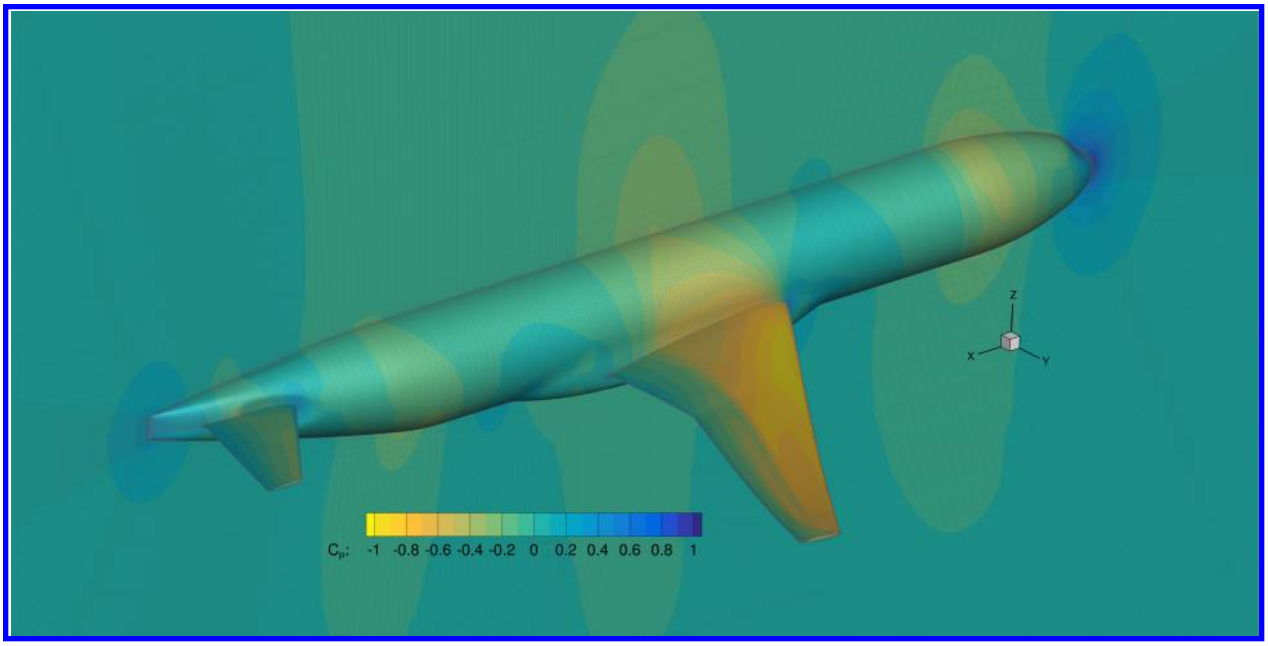


Figure 4: uCRM wing-body-tail CFD solution and mesh used to generate loads.

($w_b = h_s$). Using this approach, we can perform panel-level buckling analysis while considering multiple buckling modes. These buckling modes include: intra-stiffener skin buckling, stiffener buckling, and coupled stiffener-skin buckling modes. All three buckling modes are aggregated into a single scalar value using a Kreisselmeier–Steinhauser (KS) function [1, 32], which gives a conservative approximation to the most violated case.

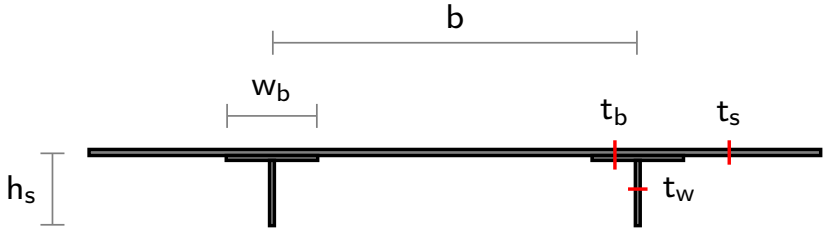


Figure 5: Panel-stiffener parametrization assumed by the smeared stiffness approach [15].

The structural sizing of the wingbox was produced through a structural optimization. The optimization consisted in minimizing the mass while enforcing failure and buckling constraints at a 2.5 g maneuver load. The skin, ribs, and spar panels were constrained not to fail or buckle with a safety factor of 1.5. The structural analysis included inertial load relief from the structure, engine, and fuel. The design variables are stiffener pitch (spacing), stiffener height, stiffener thickness, and panel thickness. The stiffener pitch for the upper and lower skins are equal everywhere. The remaining structural variables are free to change (within their bounds) from one panel to the next. Figure 6 shows the panel definition distribution across the primary wing structure. This initial optimized wingbox provides an initial guess for the structure of the wing jig shape. However, because this first guess is based on the CRM OML it also features the "built-in" 1 g deflection in its geometry. We remove this deflection in the subsequent inverse design procedure, so that the CRM wing geometry can be recovered from the jig through structural deflection of the wingbox.

### D. Jig OML and Wingbox

Given the 1 g OML of the original CRM, the wingbox structural layout and sizing, as well as the aerodynamic loads, we determine the jig shapes for the OML and wingbox. This is accomplished by solving a least square optimization problem where we minimize the difference between the CRM OML points, $X_T$, and points on the deflected jig shape

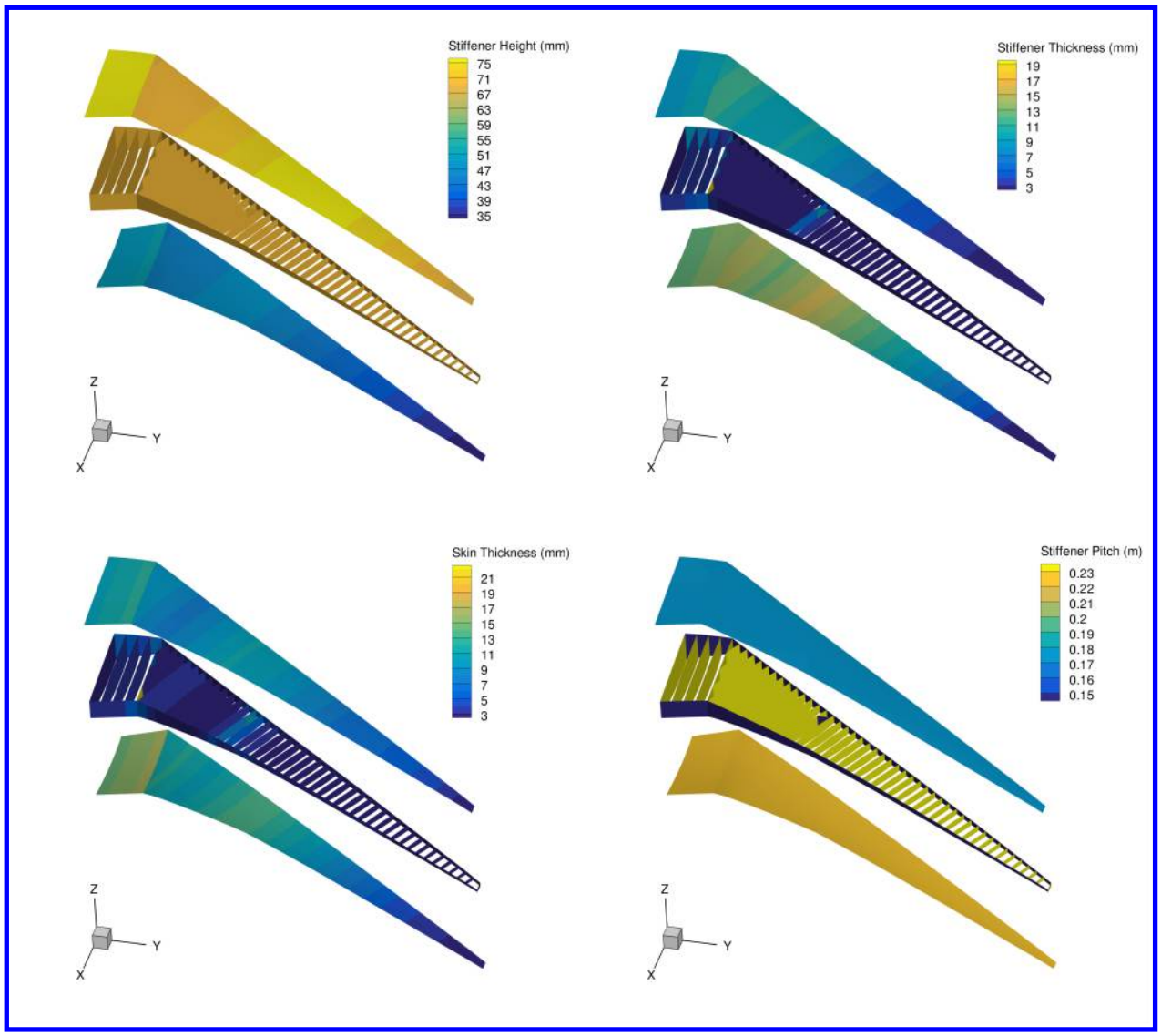


Figure 6: Distribution of stiffener height, stiffener thickness, skin thickness, and stiffener pitch for the uCRM-9 structural design.

under the nominal 1 g loads, $X_{\text{deflect}}$. The deflected points are found by taking the jig points and adding the structural deflections from the applied aerodynamic loads ($X_{\text{deflect}} = X_{\text{jig}} + u$). The optimizer change only the geometry of the wing jig through the FFD $x$, $y$, and $z$ coordinates to match the two sets of points. The goal is to match the two sets of points such that the initial deflection of the CRM wing is achieved through structural deflection only. Once the FFD shape variables are found we apply them to the initial CRM geometry and wingbox to remove the deflection and achieve a new approximate jig geometry. The new structural geometry is then structurally resized using another structural optimization and the procedure is repeated until convergence. In our case, three inverse design cycles were required before a converged jig solution was achieved. Figure 7 shows the sequence of inverse design results leading to the finalized wing jig. The final structure of the wingbox, including both wings, was 23 916 kg. We dubbed the final wing jig and structural geometry as the uCRM-9.

To verify the resulting jig shapes and wingbox sizing, we perform an aerostructural analysis of the uCRM-9 and compare it to the aerodynamic analysis of the CRM. Figure 8 shows a comparison of the upper surface $C_p$ contours and aerodynamic coefficients of interest. From these results, we find that the $C_p$ distributions are in good agreement, although there are slight differences that can be attributed to the 0.04 deg angle of attack difference in the aerostructural solution. This difference in angle of attack was necessary to match the lift coefficient of the original CRM case. The drag coefficient values differ by roughly 0.1%, which we consider to be acceptable given the additional complexity

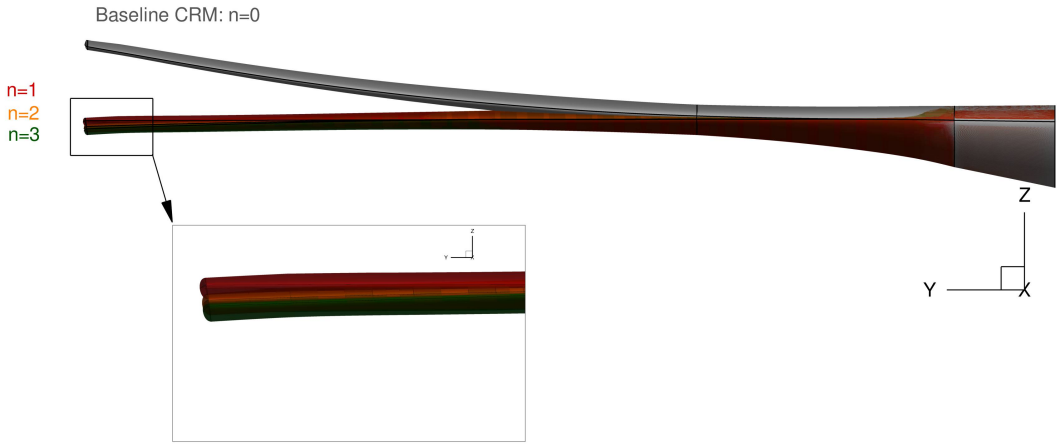


Figure 7: Inverse design iteration history for uCRM-9 wing jig.

of the aerostructural solution. Although the two models are in good agreement at the nominal cruise condition, the aerostructural analysis depends on the load transfer scheme used to couple the aerodynamic and structural solvers, as well as the aerodynamic and structural solvers themselves. This can lead to a source of discrepancy in the aerostructural solutions from solver to solver. However, we believe that uCRM-9 is a representative model for aerostructural and aeroelastic design studies.

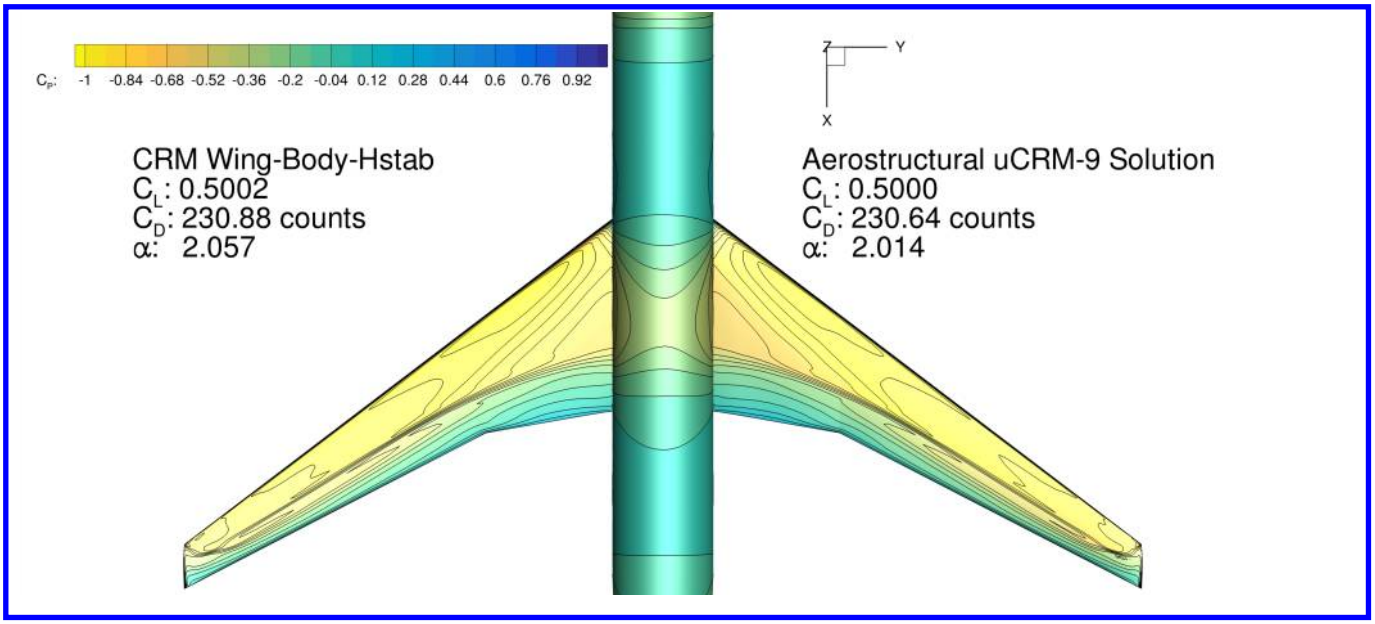


Figure 8: $C_p$ contours comparison of original CRM geometry CFD solution and uCRM aerostructural solution.

## V. uCRM-13.5 Definition

The uCRM-13.5 model is the result of a full aerostructural design optimization where the OML is optimized in addition to the structural sizing. This is in contrast with the uCRM-9 model, where the CRM OML is preserved, and only a structural sizing optimization is performed. The uCRM-13.5 wing maintains overall compatibility with

the remainder of the CRM aircraft. In this way, the resulting aircraft design may be considered to be a higher span derivative of the CRM. The goal of his model is to develop a straightforward modification of the well-tested CRM configuration with a clear connection to that configuration. The extension of the uCRM-9 to obtain the required 13.5 aspect ratio is complicated by the fact that we want to preserve the same wing loading and landing gear location to avoid a cascade of design changes that would affect the preliminary sizing. Keeping in mind the constraints imposed by a common fuselage, empennage, and propulsion system, we decided to keep the planform area fixed.

### A. Planform and General Characteristics

The uCRM-13.5 wing planform was designed by first taking the uCRM-9 planform and extending the wing span until an aspect ratio of 13.5 was achieved. The wing Wimpress area was kept constant, to ensure that the wing loading remained unchanged. A graphical representation of the Wimpress area calculation is shown in Figure 9.

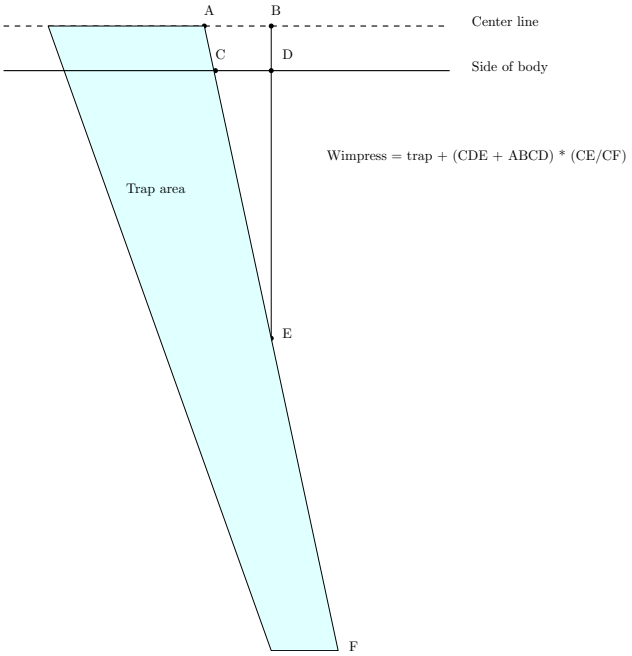


Figure 9: Wimpress area definition.

The 13.5 aspect ratio is based on the Wimpress area as it had been for the uCRM-9 configuration. While the Wimpress area has remained essentially unchanged, the gross wing area (full projected area, included area covered by the fuselage) increased by 12.9%. These area increases are caused by the larger Yehudi break area required to meet the landing gear post constraint. The uCRM-13.5 has a smaller taper ratio of 0.25 compared to the 0.275 value of the uCRM-9. This smaller taper ratio facilitates meeting other design constraints. The Yehudi break spanwise location was moved from 37% to 40% span to ensure adequate space for the landing gear. Unlike the uCRM-9, the uCRM-13.5 trailing edge is perfectly aligned with the $y$-axis inboard of the Yehudi break, similarly to the Boeing 777 planform. Figure 10 shows the uCRM-13.5 planform in comparison with uCRM-9.

To minimize the change in aircraft longitudinal stability characteristics, the entire uCRM-13.5 planform is shifted forward to align the 1/4 chord MAC location with the uCRM-9 reference point location (also at the 1/4 chord MAC location). This leaves the nominal moment arm of the horizontal and vertical stabilizers unchanged. This also has the additional benefit of distributing the delta in side of body chord to the leading and trailing edges, minimizing the required changes to the wing body fairing. A three-view rendering of the uCRM-13.5 planform is shown in Figure 11. Note that the in-built dihedral present in the uCRM-9 has been removed. The key geometric parameters of the uCRM-9 and uCRM-13.5 planforms are listed in Table 3.

The structural wingbox planform is shown in Figure 11. We designed the uCRM-13.5 wingbox to have the same topology as the uCRM-9, with the exception of the number of ribs. The absolute spacing was kept the same, and hence the uCRM-13.5 has 9 additional ribs for a total of 54. The trailing edge spar also features a more distinctive kink at the Yehudi break. This was done to move the spar forward in this region and ensure that the spar depth did not become so small as to become a manufacturing concern. The engine is also assumed to be mounted in the same absolute spanwise position.

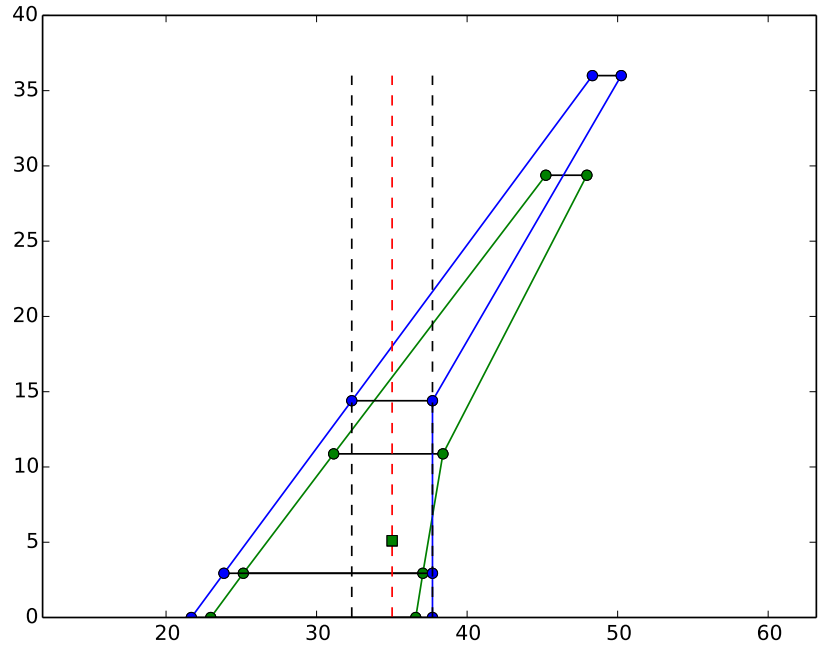


Figure 10: uCRM-13.5 wing planform (blue) and CRM-9 planform (green). The dotted lines show the 0%, 50% and 100% MAC locations for the uCRM-13.5. The green dot on the 50% MAC location signifies the main gear post.

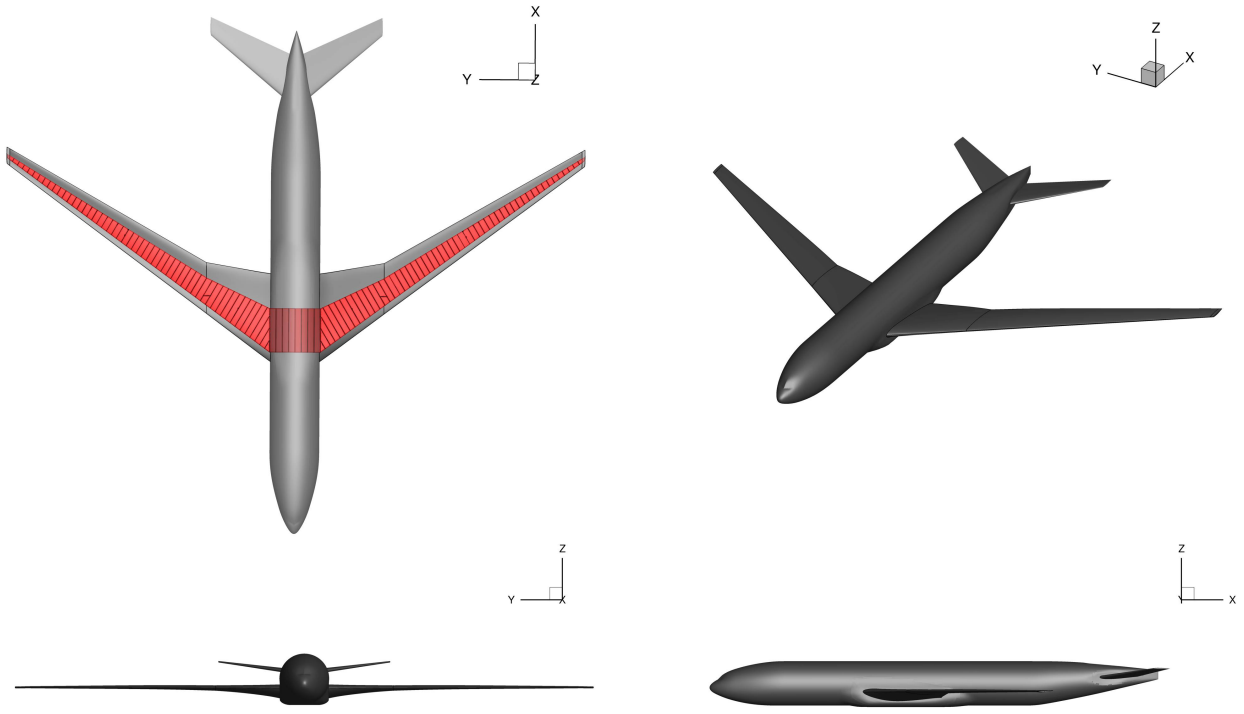


Figure 11: Three view of the uCRM-13.5 wing planform and structural geometry.

Table 3: uCRM specifications

| Parameter | uCRM-9 | uCRM-13.5 | Units |
|---|---|---|---|
| Aspect ratio | 9.0 | 13.5 | |
| Span | 58.76 | 72.00 | m |
| Root chord | 13.62 | 16.02 | m |
| Side of body chord | 11.92 | 13.85 | m |
| Yehudi chord | 7.26 | 5.36 | m |
| MAC | 7.01 | 5.36 | m |
| Tip chord | 2.73 | 1.915 | |
| Wimpress reference area | 383.74 | 384.05 | $m^2$ |
| Gross area | 412.10 | 465.22 | $m^2$ |
| Exposed area | 337.05 | 377.45 | $m^2$ |
| 1/4 chord sweep | 35 | 35 | deg |
| Taper ratio | 0.275 | 0.250 | |
| Gear post depth | 0.736 | 0.648 | m |



## B. uCRM-13.5 Aerostructural Design Optimization Description

Like the uCRM-9 design, we based the uCRM-13.5 on a traditional aluminum wingbox structure. A 13.5 AR wing is pushing the limits of what is currently possible with conventional aluminum wing design. As a result, if we perform an aerostructural analysis of this model while keeping a similar cross-sectional, twist, and structural sizing distribution as the uCRM-9, the design performs poorly due to the additional structural deformation caused by the increased wing flexibility. For this reason, unlike for uCRM-9, we use an aerostructural design optimization that takes these effects into account to achieve a meaningful baseline for the uCRM-13.5 model. Buffet onset constraints were also included for the design optimization to obtain a wing that can be used for a transonic transport. In this section, we provide a complete description of the design optimization problem that we used to obtain the uCRM-13.5 benchmark model. The initial wing weight is estimated from a structural optimization preformed prior to the aerostructural optimization. For the optimization, the structural model uses second-order MITC shell elements resulting in 190 710 total degrees of freedom. The CFD mesh used to compute the aerodynamics was an overset mesh consisting of roughly 1.2 million volume cells.

The flight conditions considered consist of a five point cruise stencil, two buffet constraint conditions, and three maneuver conditions. Details of the initial optimization flight conditions are included in Table 4, where MTOW is the maximum takeoff weight of the aircraft. The five cruise design conditions form a cross in Mach-$C_L$ space. This is done to ensure that the fuel burn of the design is robust for varying aircraft weights and flight conditions. The center of the cruise stencil, condition 1, is defined by the nominal CRM cruise condition (Mach $= 0.85, C_L = 0.5$). Conditions 2 and 3, are defined as offsets of $\pm 0.025$ in $C_L$ relative to nominal cruise condition. Conditions 4 and 5 are defined as offsets of $\pm 0.01$ in Mach number relative to the nominal condition, with the constraint that they maintain the same physical lift. The two buffet conditions are chosen to constrain buffet due to high lift and due to high Mach. The first buffet point is specified to be a 1.3 g margin on the highest lift at cruise (condition 3). The second buffet condition is placed at a high Mach design point ($M = 0.89$) with the constraint that the lift match that of the nominal cruise (condition 1). All buffet and cruise conditions are evaluated at an altitude of 37,000 ft. The three maneuver conditions consist of $-1$ g, and 2.5 g, maneuver conditions, and a 1 g cruise gust condition where failure (yield stress) and buckling constraints are enforced. The optimization problem is summarized in Table 5.

### *1. Objective*

The objective of the optimization is to minimize the average fuel burn at the cruise conditions. For this optimization, the fuel burned during the taxiing, take-off, climb, and descent phases of the flight are neglected. The fuel burn for each cruise condition, $\text{FB}_i$, is computed using the Breguet range equation,

$$\text{FB}_i = \text{LGW}\left(\exp\left(\frac{R\,\text{TSFC}}{V_i\ (L/D)_i}\right) - 1\right), \tag{1}$$

where LGW is the aircraft landing weight, $R$ is the range, TSFC is the thrust-specific fuel consumption of the engine, and $V_i$ and $(L/D)_i$ are the flight speed and lift-to-drag ratio at the $i$-th cruise condition, respectively. Since the model does not include the vertical tail or engine nacelles and corresponding pylons, 35 counts of drag are added to

Table 4: Initial flight condition stencil

| Number | Condition | FB Weight ($T_i$) | Mach | $C_L$/Lift | Altitude (ft) |
|---|---|---|---|---|---|
| 1 | Cruise | $1/5$ | 0.85 | 0.5 | 37 000 |
| 2 | Cruise | $1/5$ | 0.85 | 0.475 | 37 000 |
| 3 | Cruise | $1/5$ | 0.85 | 0.525 | 37 000 |
| 4 | Cruise | $1/5$ | 0.84 | 0.512 | 37 000 |
| 5 | Cruise | $1/5$ | 0.86 | 0.488 | 37 000 |
| 6 | Buffet | 0 | 0.85 | 0.683 | 37 000 |
| 7 | Buffet | 0 | 0.89 | 0.456 | 37 000 |
| 8 | 2.5 g Maneuver | 0 | 0.64 | $2.5 \cdot$ MTOW | 0 |
| 9 | $-1$ g Maneuver | 0 | 0.64 | $-$MTOW | 0 |
| 10 | Cruise w/ gust | 0 | 0.86 | MTOW | 27 300 |

the CFD computed drag coefficient to account for these missing components. The landing weight of the aircraft is computed from the wingbox finite-element model along with a set of fixed weight components—fuselage, payload, non-structural masses, etc.—using the following formula:

$$\text{LGW} = 1.25 \times W + \text{Fixed Weight} + \text{Reserve Fuel Weight} + \text{Secondary Wing Weight}, \tag{2}$$

where $W$ is the weight computed by the wingbox structural model. The factor of 1.25 accounts for additional weight associated with fasteners, overlaps, and other components not modeled in the idealized wingbox. Table 6 list other design parameters used to compute the objective function.

### 2. *Design Variables*

To take full advantage of gradient-based high-fidelity design optimization, many design variables is required. A total of 1112 design variables are used for this design optimization. These design variables can be broken down into three groups: geometric variables, aerodynamic variables, and structural variables. There variables are listed in Table 5. The geometric design variables include the airfoil cross-sectional shape distribution over the span of the wing. The optimizer controls these shapes by perturbing the $z$-coordinate of each control points along the FFD surface containing the wing, shown as red spheres in Figure 1. The optimizer also controls the spanwise twist distribution of the wing by rigidly rotating set of chord-wise FFD control points. The optimizer cannot change the planform (sweep, span, and reference area), because we want to keep it fixed for the design.

The aerodynamic design variables include the angle of attack for each of the 10 flight conditions. The angle-of-attack variables are necessary to satisfy the lift constraint for each condition. In addition to the angle-of-attack variables, we also include a horizontal stabilizer incidence angle variable for each flight condition. This variable makes sure that we can trim out the pitching moment about the aircraft center of gravity for each flight condition. Finally, a target nominal lift coefficient variable was added to allow the nominal cruise condition to change to ensure an optimal cruise $C_L$. The other four flight conditions follow this changing nominal condition using the specified $C_L$ variations. Only the cruise and buffet points were affected by the moving stencil, the maneuver conditions were constrained to match the aircraft MTOW. The purpose of allowing the optimizer to move the position of the cruise stencil in $C_L$ was to in effect give control over the design cruise altitude. This means that as the nominal cruise $C_L$ increases, the aircraft has to fly at a higher cruise altitude to carry the same weight.

The remaining design variables consist of the structural design variables used to parameterize the wingbox. These include the stiffener pitch of the upper skin, lower skin, leading edge spar, and trailing edge spar, since the pitch is assumed to be constant across each of these components. As a result of the panel-based smeared stiffness approach, described in Section IV, three additional design variables are added for each wingbox rib bay section: panel thickness, stiffener thickness, and stiffener height. The only exception to this are the ribs, all of which share stiffener design variables. Additionally, the panel length is included as a design variable for each panel to simplify panel buckling computations. Since the panel dimensions change with the geometry during the optimization, a nonlinear consistency constraint must be added for each panel length variable to ensure that they match the respective geometric panel lengths of each component.

Table 5: Buffet-constrained aerostructural optimization problem used to define the uCRM-13.5 baseline.

| | Variable/function | Description | Quantity |
|---|---|---|---|
| minimize | $\sum_{i=1}^{N} T_i \text{FB}_i$ | Average Fuel Burn | |
| with respect to | $x_{\alpha_i}$ | Angle of attack for each case | 10 |
| | $x_{\text{tail}}$ | Tail trim angle for each case | 10 |
| | $x_{\text{twist}}$ | Wing twist | 8 |
| | $x_{\text{airfoil}}$ | FFD control points | 240 |
| | $x_{\text{thick}}$ | Panel thickness skin/spars/ribs | 287 |
| | $x_{\text{stiff thick}}$ | Panel stiffener thickness skin/spars/ribs | 184 |
| | $x_{\text{stiff height}}$ | Panel stiffener height skin/spars/ribs | 184 |
| | $x_{\text{panel length}}$ | Panel length skin/spars/ribs | 184 |
| | $x_{\text{stiff pitch}}$ | Panel stiffener pitch skin/spars/ribs | 4 |
| | $C^*_{L_0}$ | Nominal cruise target lift coefficient | 1 |
| | | **Total design variables** | **1112** |
| subject to | $C_{L_i} = C^*_{L_i}$ | Cruise and Buffet lift conditions | 7 |
| | $L = n_i W$ | Maneuver lift conditions | 3 |
| | $c^i_{m_y} = 0$ | Trimmed flight | 10 |
| | $t_{\text{LE}}/t_{\text{LE}_{\text{init}}} \geq 1.0$ | Leading edge radius | 20 |
| | $t_{\text{TE}}/t_{\text{TE}_{\text{init}}} \geq 1.0$ | Trailing edge thickness | 20 |
| | $(t/c)_{\text{TE,spar}} \geq 0.80(t/c)_{\text{TE spar}_{\text{init}}}$ | Minimum trailing edge spar height | 20 |
| | $L_{\text{panel}} - x_{\text{panel length}} = 0$ | Target panel length | 266 |
| | $\text{KS}_{\text{fail}} < 1.0$ | 2.5 g Material Failure | 8 |
| | $\text{KS}_{\text{buckling}} < 1.0$ | 2.5 g and -1 g Buckling | 9 |
| | $\left\lvert x_{\text{panel thick}_i} - x_{\text{panel thick}_{i+1}} \right\rvert \leq 0.0025$ | Skin thickness adjacency | 258 |
| | $\left\lvert x_{\text{stiff thick}_i} - x_{\text{stiff thick}_{i+1}} \right\rvert \leq 0.0025$ | Stiffener thickness adjacency | 258 |
| | $\left\lvert x_{\text{stiff height}_i} - x_{\text{stiff height}_{i+1}} \right\rvert$ | Stiffener height adjacency | 258 |
| | $x_{\text{stiff thick}} - x_{\text{panel thick}} < 0.005$ | Maximum stiffener-skin difference | 172 |
| | $\Delta z_{\text{TE,upper}} = -\Delta z_{\text{TE,lower}}$ | Fixed trailing edge | 8 |
| | $\Delta z_{\text{LE,upper}} = -\Delta z_{\text{LE,lower}}$ | Fixed leading edge | 8 |
| | $\text{Sep}_i \leq 0.04$ | Buffet separation constraints | 2 |
| | | **Total constraints** | **1327** |

Table 6: Design optimization specifications

| Parameter | Value | Units |
|---|---|---|
| Initial cruise altitude | 37 000 | ft |
| Initial Maximum take-off weight (MTOW) | 297 500 | kg |
| Maximum landing weight (MLW) | 213 180 | kg |
| Maximum zero fuel weight (MZFW) | 195 040 | kg |
| Operational empty weight | 138 100 | kg |
| Design range | 7 725 | nm |
| Design payload | 34 000 | kg |
| Reserve fuel | 15 000 | kg |
| Initial wing weight | 30 286 | kg |
| Fixed weight | 107 814 | kg |
| Thrust specific fuel consumption ($c_T$) | 0.53 | lb/(lbf · h) |

### 3. Constraints

To achieve a meaningful and physically realizable design, many constraints must be considered for the optimization problem. In total, our design optimization enforces 1327 linear and nonlinear constraints. The first of these constraints is to ensure a steady flight for each design condition. For the cruise and buffet conditions this means that the lift coefficient, $C_{L_i}$, for that condition must match the value defined by the moving cruise flight conditions stencil. For the maneuver conditions, the constraint is specified for the physical lift, such that the lift equals the MTOW multiplied by the respective load factor, $n$, where the MTOW is based on the fuel burn computed from the first cruise condition as shown below:

$$\text{MTOW} = \text{LGW} + \text{FB}_0. \tag{3}$$

As mentioned previously, each flight condition is also constrained to be trimmed (zero moment) about their respective centers of gravity. Additionally, we have a separation-based buffet constraint for the two buffet design points. By constraining these two points, we ensure that all cruise points remain in the envelope defined by the 1.3 g margin to buffet onset, as required by flight regulations [**?** ].

The next set of constraints are applied to the geometry of the design to prevent the optimizer from arriving at physically unrealizable designs. There is a constraint on the wing leading edge radius preventing it from decreasing relative to the baseline. This is done to prevent the optimizer from compromising the aircraft high-lift performance for takeoff and landing, which are not included in the optimization. Lyu et al. [29] showed that transonic wing optimizations without this constraint yield designs with unrealistically sharp leading edges. Additionally, a constraint is applied to the wing trailing edge to preventing the thickness from decreasing. This is done to prevent the optimizer from producing designs with excessively thin trailing edges, which lead to manufacturing difficulties. Similar to the trailing edge, a constraint is placed on the depth of the wing at the location of the trailing edge spar. This is done, again, to prevent manufacturing difficulties, as well as to ensure that there is adequate room for the actuators and control surfaces to be mounted on the spar. There is a volume constraint on the fuel bay of the wing that ensures that there is enough volume for the fuel required to complete the mission, including reserve fuel. The last of the sets of geometric constraints consists of 16 linear constraints on the FFD shape variables that prevent the leading edge to move vertically relative to the trailing edge. This ensures that no inadvertent twist is added to the wing through the shape variables, and guarantees that the twist and shape variables are independent.

The remaining constraints are applied to the structure of the wing. The 2.5 g maneuver and 1 g cruise with gust conditions each use four KS material failure constraint aggregation functions: one each for the upper skin, lower skin, ribs, and spars. For these conditions, aggregated buckling constraints are enforced only for the upper skin, ribs, and spars. For the $-1.0$ g condition, only the buckling constraints are enforced for the lower skin, ribs, and spars. This is because the $-1.0$ g case is not critical in sizing for stress like the 2.5 g and 1 g cruise condition. As mentioned previously, there are also consistency constraints for each panel to ensure that the panel length used for the buckling calculations are consistent with the physical dimensions of the panel. Finally, we apply hundreds linear adjacency constraints to ensure that the panel thickness, and stiffener thickness and heights do not change too much from panel to panel.

## C. Results

In addition to the uCRM-13.5 baseline design produced by the optimization procedure described in the previous section, we also develop three additional designs as a reference. The first reference design is the result of an optimization of the uCRM-13.5 planform where only a single cruise condition is considered, and buffet onset was not constrained. This is done to assess the effect of the multipoint cruise analysis and buffet constraints had on the design. The remaining two reference designs are based on the uCRM-9. One of these is an aerostructural analysis of the uCRM-9 baseline design, defined in the previous section. The final design is developed by starting with the uCRM-9 baseline and optimizing using same buffet-constrained multipoint aerostructural optimization design procedure used to obtain the uCRM-13.5 baseline. The goal of the last design is to assess the effect that the higher aspect ratio wing had on the designs performance.

For the uCRM-9 based optimization, the CFD volume mesh and structural mesh were adjusted to 1.2 million cells and 120 000 degrees of freedom respectively, to be comparable with the size of the meshes used for the uCRM-13.5 optimizations. The buffet constrained multipoint optimizations were run on 1,000 processors (roughly 100 processors per flight condition) for up to 48 hours. The iteration histories for the three optimizations are plotted in Figure 12. The objective function is the fuel burn in percent of the design MTOW. The feasibility and optimality are a measurement of the constraint violation and satisfaction of the first order Karush-Kuhn-Tucker (KKT) conditions, respectively [11]. In all three cases the optimizer gradually reduces the objective while improving the feasibility of the design.

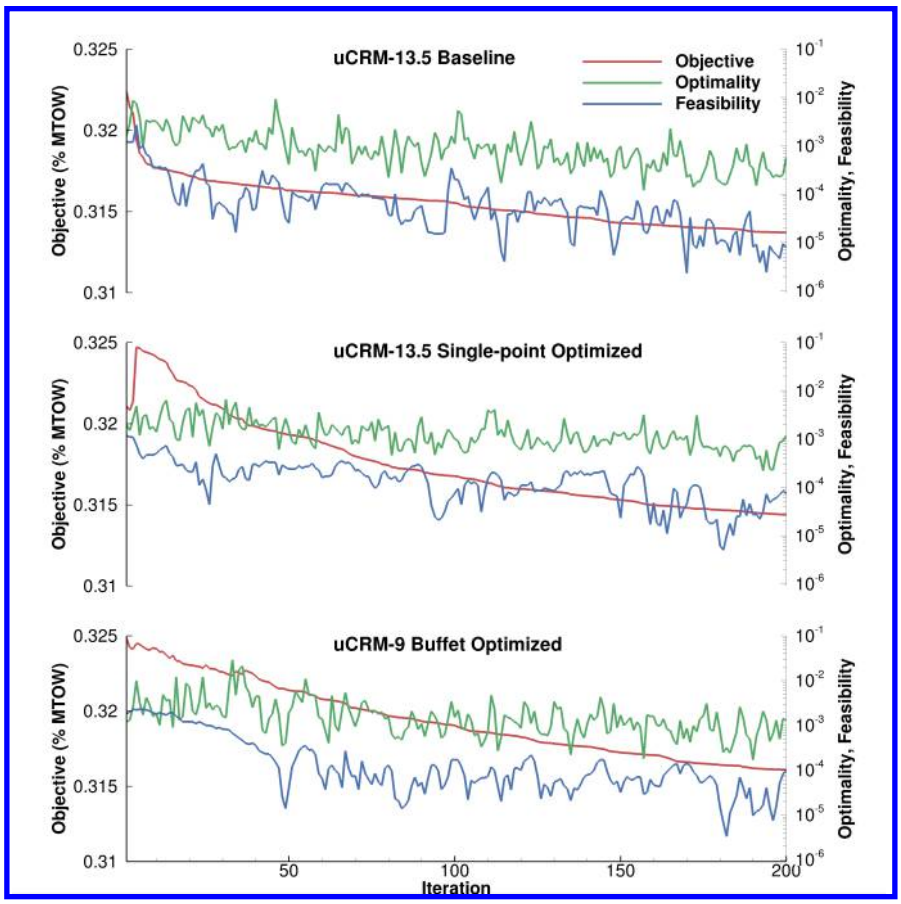


Figure 12: Optimization convergence histories for the each cases

Figures 13 and 14 compare the two uCRM-13.5 based designs and the two uCRM-9 based designs, respectively. In the top left corner of these figures we have the cruise $C_p$ distribution of each design, as well as a front view with the deflection of the wing at various flight conditions. Below that we have spanwise aerodynamic quantities of interest: normalized lift distribution, wing twist, and wing thickness to chord ratio. On the upper right hand corner we have the structural values of interest: mass equivalent structural thickness distribution of the wingbox panels, as well as the buckling and material failure constraints for the 2.5 g maneuver condition (the most restrictive of the maneuver conditions) over each wingbox component. Finally, below this we have four airfoil slices and corresponding $C_p$ distributions at various spanwise locations along the wing. Additionally, both buffet optimized designs were free to translate their cruise and buffet design conditions with respect to $C_L$ during the optimization. The final flight conditions from the uCRM-13.5 and uCRM-9 buffet optimizations are listed in Table 7 and 8, respectively.

Comparing the uCRM-13.5 baseline (buffet optimized) and single point optimized designs in Figure 13, we find a similar performance in fuel burn, with only a 0.2% improvement in the baseline aircraft's favor. Looking at the $L/D$ value, we see that the baseline design outperforms the single point aerodynamically. This is due to the fact that the baseline design is given the freedom to change the $C_L$ of its design points, whereas the single-point design was constrained to the nominal value of $C_L = 0.5$. The single point design makes up for this fact by lowering the structural weight by roughly 10% such that the two designs still en up with roughly the same fuel burn.

Comparing the uCRM-9 baseline and buffet optimized designs in Figure 14, we find that the buffet optimized design was able to reduce the fuel burn of the design by 3.7% (3,603 kg). Looking at the structural weight of both designs, we find that the structural weight of the wing remains largely unchanged. This is despite a significant reduction in the wing thickness distribution over the span for the buffet-optimized design. If we look at the normalized lift distribution for these designs, we find that the optimizer accomplishes this by shifting the maneuver load in-board, which reduces the structural load at the root of the wing while maintaining elliptical lift distribution during cruise to reduce drag. This is a concept known as passive load alleviation, and is enabled by the structural bend-twist coupling inherent ion sweptback wings. The reason the buffet-optimized design reduces the $t/c$ distribution of the wing relative

to the baseline is largely due to aerodynamics. A lower $t/c$ is favorable for reducing the onset of flow separation on the design which in turn helps meet the buffet onset constraint. This allows the buffet-optimized design to fly at a slightly higher $C_L$, which improves the $L/D$.

By comparing between the AR 13.5 designs in Figure 13 with the AR 9 designs in Figure 14, we find a significantly better fuel burn performance: 10% (10,000 kg), for the higher aspect ratio wing designs. This makes sense because the longer span reduces the induced drag, thereby improving the aerodynamic performance. This is despite the significant structural weight penalty associated with the higher aspect ratio wing designs in wing mass (9%, 2,800 kg). By looking at the structural thickness distribution along the panels of the wingbox, we see that the difference in weight comes from a noticeably thicker wingbox near the Yehudi break of the wing. Again, this makes sense because the longer span of the AR 13.5 designs also means a larger moment arm for the aerodynamic loads, which increases the internal forces in the wing, requiring more structural material. Comparing the normalized lift distribution between each deign, we find that the lower aspect ratio wings achieve a more elliptical lift distribution during cruise flight, while the higher aspect ratio wings shift the load more in board. This is because the structural weight penalty associated with an elliptical spanwise wing loading outweighs the aerodynamic benefit due to the lower drag for the larger span wings.

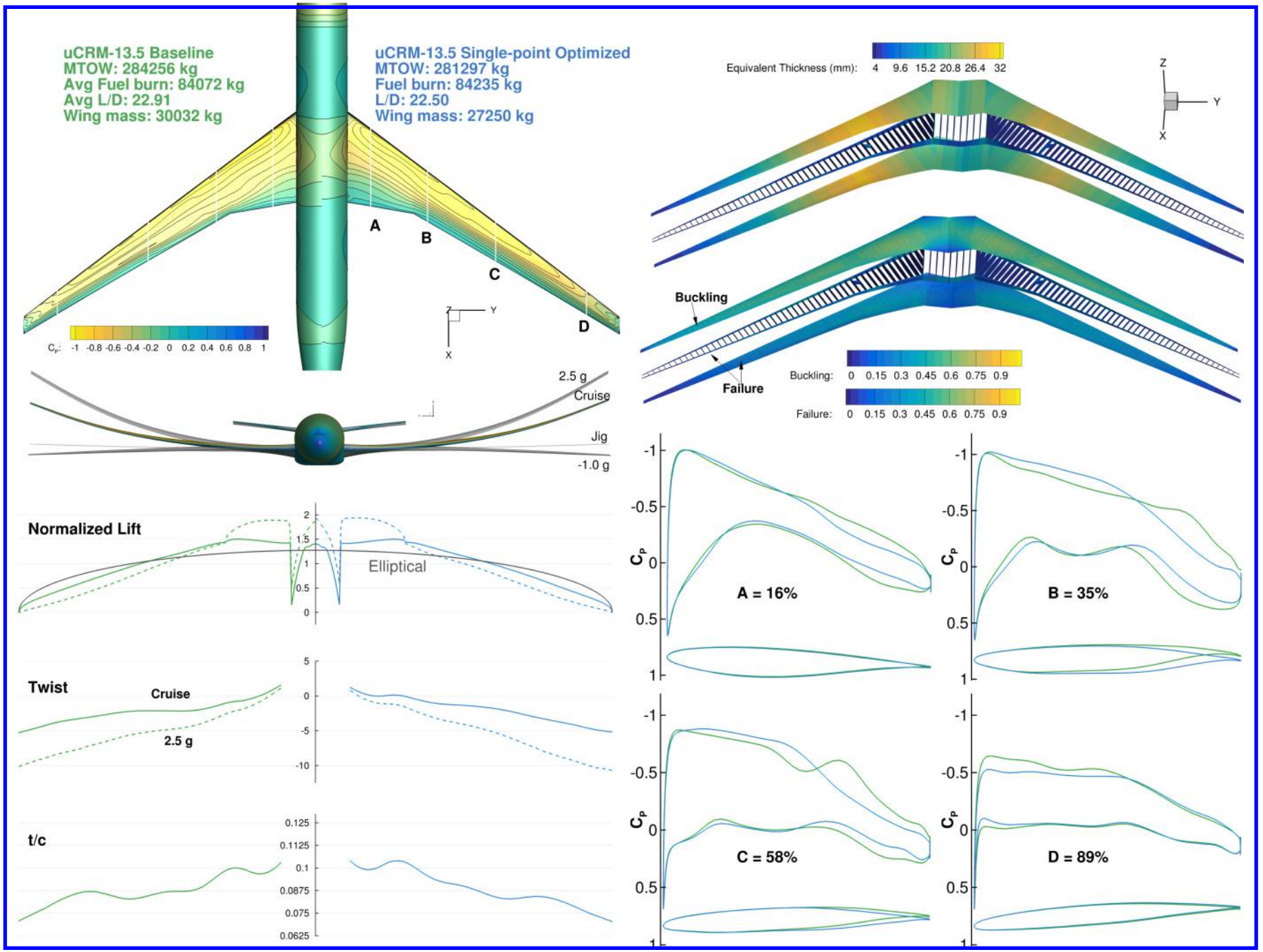


Figure 13: Comparison of finalized uCRM-13.5 baseline (left) with single-point optimized uCRM-13.5 (right) aerostructural design

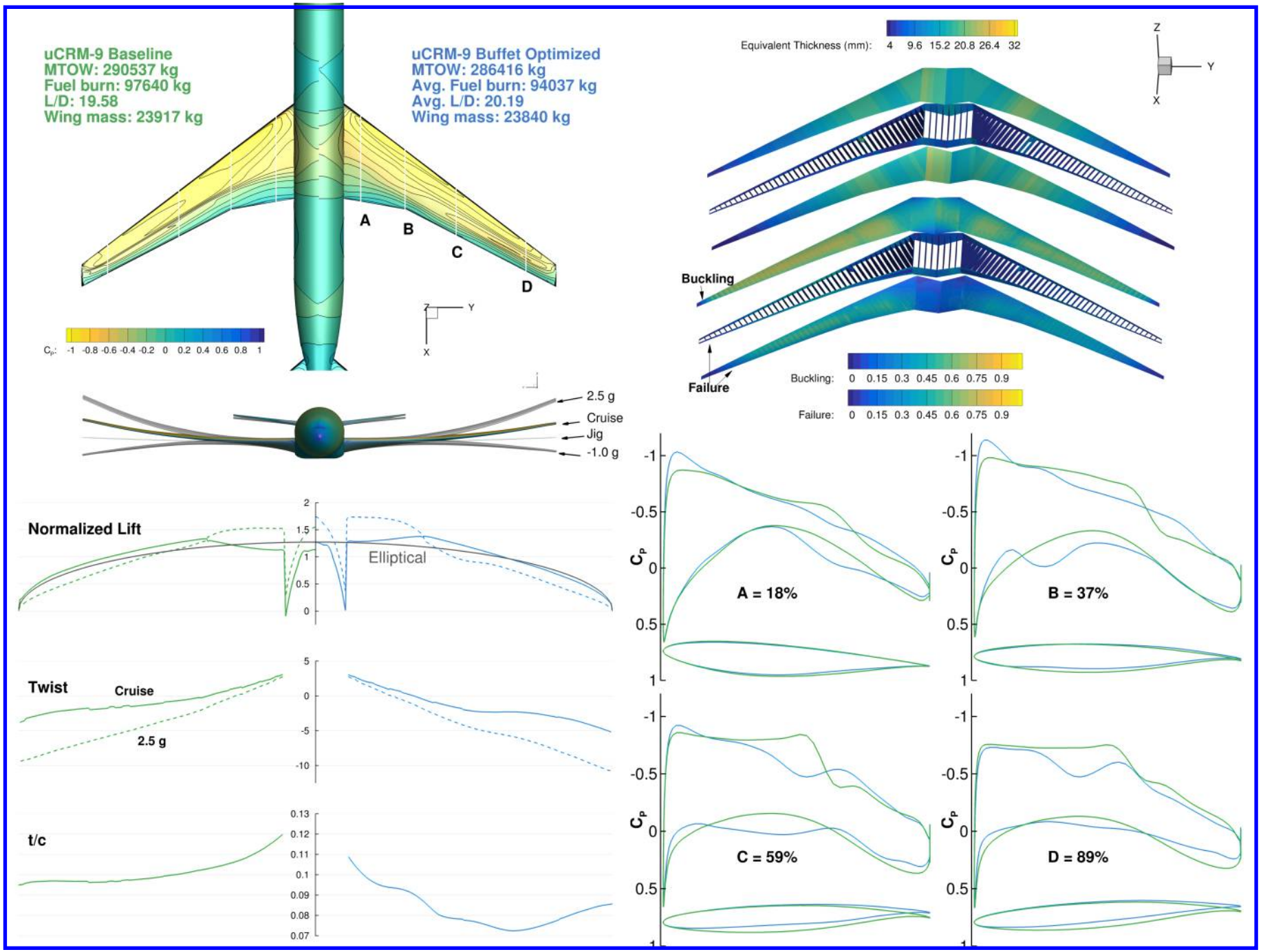


Figure 14: Comparison of the finalized uCRM-9 baseline (left) with buffet-optimized uCRM-9 (right) aerostructural design

Table 7: uCRM-13.5 baseline final flight condition stencil

| Point | Condition | Mach | $C_L$ |
|---|---|---|---|
| 1 | Cruise | 0.85 | 0.549 |
| 2 | Cruise | 0.85 | 0.524 |
| 3 | Cruise | 0.85 | 0.574 |
| 4 | Cruise | 0.84 | 0.562 |
| 5 | Cruise | 0.86 | 0.536 |
| 6 | Buffet | 0.85 | 0.746 |
| 7 | Buffet | 0.89 | 0.501 |

Table 8: Buffet-optimized uCRM-9 final flight condition stencil

| Point | Condition | Mach | $C_L$ |
|---|---|---|---|
| 1 | Cruise | 0.85 | 0.515 |
| 2 | Cruise | 0.85 | 0.490 |
| 3 | Cruise | 0.85 | 0.540 |
| 4 | Cruise | 0.84 | 0.527 |
| 5 | Cruise | 0.86 | 0.503 |
| 6 | Buffet | 0.85 | 0.702 |
| 7 | Buffet | 0.89 | 0.470 |



Figure 15 shows a fuel burn contour plot as a function of Mach and $C_L$ for both designs. This plot corresponds to different flight performance for the design at varying flight speeds and aircraft weights. This plot allows us to see both the robustness of the design and the margin between buffet onset and the cruise flight envelope. The line denoted as 1.3 g buffet boundary shows the boundary for all of the operational conditions that have a 1.3 g margin to buffet onset. Ideally, all points in the cruise stencil should lie below this line. We can see that the optimized cruise condition for the single point optimized uCRM-13.5 design is not within this feasible region. This is not a surprise, since buffet onset is not constrained for this optimization. The uCRM-9 baseline design cruise point is also slightly outside of the 1.3 g buffet region, but noticeably less so than the single point case. We find that on the buffet optimized uCRM-9 design, the optimizer increases the feasible region, allowing the optimizer to move these points to higher $C_L$ to achieve a better performance. As mentioned previously, this is made possible by an overall decrease in the spanwise $t/c$ distribution on the buffet optimized uCRM-9 design.

The other point of interest in Figure 15 is the box under the 1.3 g buffet boundary line, which is designated the fuel burn performance integration region. In this region, the fuel burn is averaged over the entire area to assess the robustness of the design. Ideally, this region should overlap with the cruise stencil, and both should lie close to the global minimum fuel burn on the plot. However, because the buffet boundary is so restrictive in single point case, the integration region is located further down in the Mach-$C_L$ design space than it should be, causing a reduction in performance. We can see that the optimizer is able to raise the performance integration region by moving the stencil up in $C_L$ on the baseline uCRM-13.5, which ultimately leads to a decrease of 9.4% (9,024 kg) in average fuel burn.

Comparing the fuel burn performance of the two uCRM-13.5 designs in Figure 15, we find that only looking at the designs performance at the optimized design points in Figure 13 leads to the false conclusion that the designs are roughly equivalent in performance. Looking at the single point optimized design, we see that while the design performance near the optimized flight condition is good, as soon as the design deviates from this condition (in Mach or lift coefficient) we pay a steep penalty in performance. This is clearly not the case for the baseline uCRM-13.5 design, since it features a flatter performance region near the optimized cruise points, where all conditions perform relatively well. This highlights the need for considering multiple flight conditions to achieve designs with robust performance. To better quantify the measurement of robustness, we also plot the contour corresponding to 101% of the minimum fuel burn of each design, in red, and compute the area enclosed by this contour. This gives us an idea of how quickly the design performance decays away from the optimal design point. Unsurprisingly, the single point uCRM-13.5 has the smallest 101% contour region. Both the uCRM-9 buffet optimized and uCRM-13.5 baseline designs improve on this considerably since they consider performance at multiple flight conditions in the optimization. The uCRM-9 has the largest 101% minimum fuel burn region, confirming this design's robustness. Once the optimization is performed, the converged wing shape and structurally sized result of the uCRM-13.5 baseline was dubbed as the uCRM-13.5 model.

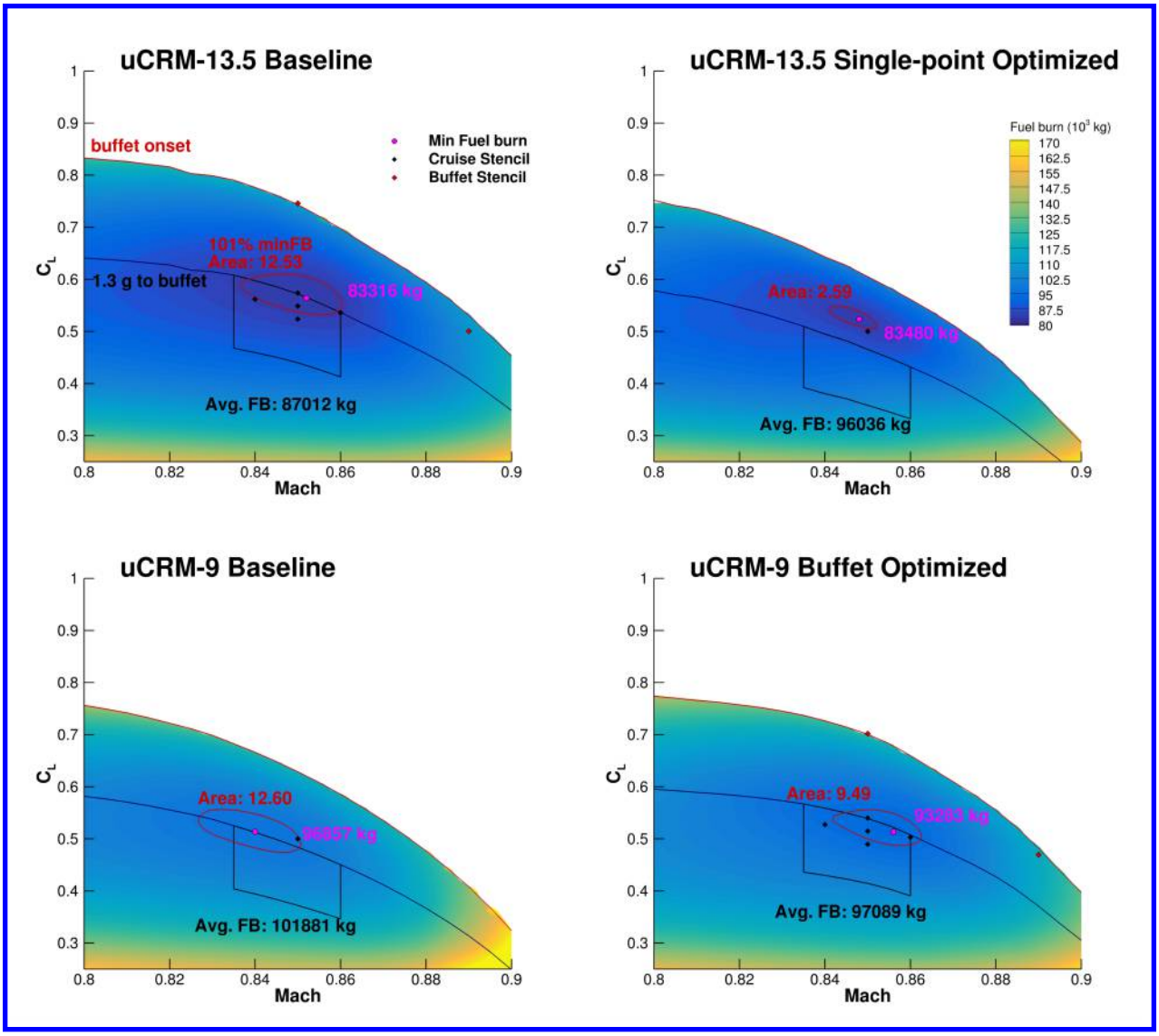


Figure 15: Fuel burn performance contours of each design as well as buffet and 1.3 g margin to buffet envelopes. The 101% minimum fuel burn contours and average integrated fuel burn performance give a measurement of each designs robustness.

## VI. Conclusions

There is currently a lack of aeroelastic models for transonic aircraft analysis and design. The NASA Common Research Model is an excellent aerodynamic model and as such is widely used as a benchmark geometry for transonic analysis. Unfortunately, due to its addition of a 1 g deflection in the wing geometry it is not appropriate as an aeroelastic model. To address the need for common aeroelastic models, we developed two baseline undeflected aeroelastic models based on the CRM geometry. The first model, the uCRM-9, is a design with an aspect ratio 9 wing that deforms into the CRM geometry under nominal cruise flight conditions. This design was obtained through an inverse design procedure. After performing an aerostructural analysis on the resulting design we found the geometry to be within 0.1% agreement with the drag produced by the CRM aerodynamic geometry.

The second aeroelastic model, the uCRM-13.5, is a higher aspect ratio variant obtained through a multipoint buffet-constrained aerostructural optimization. The motivation for this model is for studies of new technology concepts with the goal of enabling higher aspect ratio wing designs. It is our intention to provide files for both the geometry and structures of these models for future use on aeroelastic studies.

## VII. Acknowledgments

The authors would like to acknowledge support from NASA through award no. NNX11AI19A. This work used the Extreme Science and Engineering Discovery Environment (XSEDE), which is supported by National Science Foundation grant number ACI-1053575 [36].

## References

[1] M. A. Akgün, R. T. Haftka, K. C. Wu, J. L. Walsh, and J. H. Garcelon. Efficient structural optimization for multiple load cases using adjoint sensitivities. *AIAA Journal*, 39(3):511–516, 2001.

[2] Anonymous. 777-200/300 airplane characteristics for airport planning. Technical Report D6-58329, Boeing Commercial Airplanes, July 1998.

[3] T. R. Brooks, G. J. Kennedy, and J. R. R. A. Martins. High-fidelity aerostructural optimization of a high aspect ratio tow-steered wing. In *57th AIAA/ASCE/AHS/ASC Structures, Structural Dynamics, and Materials Conference*. American Institute of Aeronautics and Astronautics, January 2016. doi:10.2514/6.2016-1179.

[4] T. R. Brooks, G. J. Kennedy, and J. R. R. A. Martins. High-fidelity multipoint aerostructural optimization of a high aspect ratio tow-steered composite wing. In *58th AIAA/ASCE/AHS/ASC Structures, Structural Dynamics, and Materials Conference*, Grapevine, TX, January 2017. American Institute of Aeronautics and Astronautics. doi:10.2514/6.2017-1350.

[5] S. A. Brown. Displacement extrapolation for CFD+CSM aeroelastic analysis. In *Proceedings of the 35th AIAA Aerospace Sciences Meeting*, Reno, NV, 1997. AIAA 1997-1090.

[6] D. Burdette, G. K. W. Kenway, Z. Lyu, and J. R. R. A. Martins. Aerostructural design optimization of an adaptive morphing trailing edge wing. In *Proceedings of the AIAA Science and Technology Forum and Exposition (SciTech)*, Kissimmee, FL, January 2015. AIAA 2015-1129.

[7] D. A. Burdette, G. K. Kenway, and J. R. R. A. Martins. Performance evaluation of a morphing trailing edge using multipoint aerostructural design optimization. In *57th AIAA/ASCE/AHS/ASC Structures, Structural Dynamics, and Materials Conference*. American Institute of Aeronautics and Astronautics, January 2016. doi:10.2514/6.2016-0159.

[8] G. Carrier, D. Destarac, A. Dumont, M. Meheut, I. S. E. Din, J. Peter, S. B. Khelil, J. Brezillon, and M. Pestana. Gradient-based aerodynamic optimization with the elsa software. In *52nd Aerospace Sciences Meeting*, Feb. 2014. doi:10.2514/6.2014-0568.

[9] S. Chen, Z. Lyu, G. K. W. Kenway, and J. R. R. A. Martins. Aerodynamic shape optimization of the Common Research Model wing-body-tail configuration. *Journal of Aircraft*, 53(1):276–293, January 2016. doi:10.2514/1.C033328.

[10] T. W. Chin and G. J. Kennedy. Large-scale compliance-minimization and buckling topology optimization of the undeformed common research model wing. In *57th AIAA/ASCE/AHS/ASC Structures, Structural Dynamics, and Materials Conference, AIAA SciTech*, 2016. doi:10.2514/6.2016-0939.

[11] P. E. Gill, W. Murray, and M. A. Saunders. An SQP algorithm for large-scale constrained optimization. *Society for Industrial and Applied Mathematics*, 47(1), 2005. URL http://www.stanford.edu/group/SOL/papers/SNOPT-SIGEST.pdf.

[12] C. V. Jutte, B. K. Stanford, C. D. Wieseman, and J. B. Moore. Aeroelastic tailoring of the nasa common research model via novel material and structural configurations. In *Proceedings of the AIAA 52nd Aerospace Sciences Meeting*, January 2014. doi:doi:10.2514/6.2014-0598.

[13] G. J. Kennedy and J. R. R. A. Martins. Parallel solution methods for aerostructural analysis and design optimization. In *Proceedings of the 13th AIAA/ISSMO Multidisciplinary Analysis Optimization Conference*, Fort Worth, TX, Sept. 2010. AIAA 2010–9308.

[14] G. J. Kennedy and J. R. R. A. Martins. A parallel finite-element framework for large-scale gradient-based design optimization of high-performance structures. *Finite Elements in Analysis and Design*, 87:56–73, September 2014. doi:10.1016/j.finel.2014.04.011.

[15] G. J. Kennedy, G. K. W. Kenway, and J. R. R. A. Martins. High aspect ratio wing design: Optimal aerostructural tradeoffs for the next generation of materials. In *Proceedings of the AIAA Science and Technology Forum and Exposition (SciTech)*, National Harbor, MD, January 2014. AIAA-2014-0596.

[16] G. K. Kenway and J. R. R. A. Martins. Buffet onset constraint formulation for aerodynamic shape optimization. *AIAA Journal*, 2016. (Submitted).

[17] G. K. W. Kenway and J. R. R. A. Martins. Multipoint high-fidelity aerostructural optimization of a transport aircraft configuration. *Journal of Aircraft*, 51(1):144–160, January 2014. doi:10.2514/1.C032150.

[18] G. K. W. Kenway and J. R. R. A. Martins. Multipoint aerodynamic shape optimization investigations of the Common Research Model wing. *AIAA Journal*, 54(1):113–128, January 2016. doi:10.2514/1.J054154.

[19] G. K. W. Kenway, G. J. Kennedy, and J. R. R. A. Martins. Scalable parallel approach for high-fidelity steady-state aeroelastic analysis and derivative computations. *AIAA Journal*, 52(5):935–951, May 2014. doi:10.2514/1.J052255.

[20] G. K. W. Kenway, G. J. Kennedy, and J. R. R. A. Martins. Aerostructural optimization of the Common Research Model configuration. In *15th AIAA/ISSMO Multidisciplinary Analysis and Optimization Conference*, Atlanta, GA, June 2014. AIAA 2014-3274.

[21] G. K. W. Kenway, N. Secco, J. R. R. A. Martins, A. Mishra, and K. Duraisamy. An efficient parallel overset method for aerodynamic shape optimization. In *Proceedings of the 58th AIAA/ASCE/AHS/ASC Structures, Structural Dynamics, and Materials Conference, AIAA SciTech Formum*, January 2017. doi:10.2514/6.2017-0357.

[22] S. Keye, O. Brodersen, and M. B. Rivers. Investigation of aeroelastic effects on the nasa common research model. *Journal of Aircraft*, 51(4):1323–1330, Apr. 2014. ISSN 0021-8669. doi:10.2514/1.C032598. URL http://dx.doi.org/10.2514/1.C032598.

[23] T. Klimmek. Parametric set-up of a structural model for fermat configuration aeroelastic and loads analysis. *Journal of Aeroelasticity and Structural Dynamics*, 3(2):31–49, 2014. doi:10.3293/asdj.2014.27.

[24] S. T. LeDoux, J. C. Vassberg, D. P. Young, S. Fugal, D. Kamenetskiy, W. P. Huffman, R. G. Melvin, and M. F. Smith. Study based on the AIAA aerodynamic design optimization discussion group test cases. *AIAA Journal*, February 2015. doi:10.2514/1.j053535.

[25] S. T. LeDoux, D. P. Young, S. Fugal, J. K. Elliott, D. S. Kamenetskiy, R. G. Melvin, and W. P. Huffman. A study based on the AIAA aerodynamic design optimization discussion group test cases. In *53rd AIAA Aerospace Sciences Meeting*. American Institute of Aeronautics and Astronautics (AIAA), January 2015. doi:10.2514/6.2015-1717.

[26] R. Liem, G. K. W. Kenway, and J. R. R. A. Martins. Multimission aircraft fuel burn minimization via multipoint aerostructural optimization. *AIAA Journal*, 53(1):104–122, January 2015. doi:10.2514/1.J052940.

[27] Z. Lyu, G. K. Kenway, C. Paige, and J. R. R. A. Martins. Automatic differentiation adjoint of the Reynolds-averaged Navier–Stokes equations with a turbulence model. In *21st AIAA Computational Fluid Dynamics Conference*, San Diego, CA, Jul. 2013. doi:10.2514/6.2013-2581.

[28] Z. Lyu, G. K. W. Kenway, and J. R. R. A. Martins. RANS-based aerodynamic shape optimization investigations of the common research model wing. In *Proceedings of the AIAA Science and Technology Forum and Exposition (SciTech)*, National Harbor, MD, January 2014. doi:10.2514/6.2014-0567. AIAA 2014-0567.

[29] Z. Lyu, G. K. Kenway, and J. R. R. A. Martins. Aerodynamic shape optimization investigations of the Common Research Model wing benchmark. *AIAA Journal*, 53(4):968–985, April 2015. doi:10.2514/1.J053318.

[30] C. A. Mader, G. Kenway, and J. R. R. A. Martins. Towards high-fidelity aerostructural optimization using a coupled ADjoint approach. In *Proceedings of the 12th AIAA/ISSMO Multidisciplinary Analysis and Optimization Conference*, Victoria, BC, Sept. 2008. AIAA 2008-5968.

[31] R. E. Perez, P. W. Jansen, and J. R. R. A. Martins. pyOpt: A Python-based object-oriented framework for nonlinear constrained optimization. *Structural and Multidisciplinary Optimization*, 45(1):101–118, January 2012. doi:10.1007/s00158-011-0666-3.

[32] N. M. K. Poon and J. R. R. A. Martins. An adaptive approach to constraint aggregation using adjoint sensitivity analysis. *Structural and Multidisciplinary Optimization*, 34(1):61–73, July 2007. doi:10.1007/s00158-006-0061-7.

[33] V. Schmitt and F. Charpin. Pressure distributions on the ONERA-M6-wing at transonic mach numbers. Technical report, Office National d'Etudes et Recherches Aerospatiales, 92320, Chatillon, France, 1979.

[34] B. K. Stanford, C. V. Jutte, and C. D. Wieseman. Trim and structural optimization of subsonic transport wings using non-conventional aeroelastic tailoring. *AIAA Journal*, 54(1):293–309, Oct. 2015. ISSN 0001-1452. doi:10.2514/1.J054244. URL http://dx.doi.org/10.2514/1.J054244.

[35] K. Telidetzki, L. Osusky, and D. W. Zingg. Application of jetstream to a suite of aerodynamic shape optimization problems. In *52nd Aerospace Sciences Meeting*, Feb. 2014. doi:10.2514/6.2014-0571.

[36] J. Towns, T. Cockerill, M. Dahan, I. Foster, K. Gaither, A. Grimshaw, V. Hazlewood, S. Lathrop, D. Lifka, G. D. Peterson, R. Roskies, J. R. Scott, and N. Wilkins-Diehr. XSEDE: Accelerating scientific discovery. *Computing in Science & Engineering*, 16(5):62–74, September 2014. doi:10.1109/MCSE.2014.80.

[37] L. Uyttersprot. *Inverse Distance Weighting Mesh Deformation*. PhD thesis, Delft University of Technology, 2014.

[38] J. Vassberg. A unified baseline grid about the common research model wing/body for the fifth aiaa cfd drag prediction workshop (invited). In *29th AIAA Applied Aerodynamics Conference*, Jul 2011. doi:10.2514/6.2011-3508.

[39] J. Vassberg and A. Jameson. Influence of shape parameterization on aerodynamic shape optimization. Technical report, Von Karman Institute, Brussels, Belgium, April 2014.

[40] J. C. Vassberg, M. A. DeHaan, S. M. Rivers, and R. A. Wahls. Development of a common research model for applied CFD validation studies. 2008. AIAA 2008-6919.